Journal of Computational and Applied Research in Mechanical Engineering
jcarme.sru.ac.ir
SRTTU
JCARME
ISSN: 2228-7922

**Research paper**

# Experimental investigation and multi-response optimization of FFF-printed PETG sandwich structure properties for battery casings

**T. J. Suteja[a,*], M. A. Hadiyat[b] and Y. B. Pratiknyo[a]**

[a]*Department of Mechanical Engineering, University of Surabaya, Surabaya, East Java, 60292, Indonesia*
[b]*Department of Industrial Engineering, University of Surabaya, Surabaya, East Java, 60292, Indonesia*

**Article info:**

**Article history:**

Received: 22/05/2026
Revised: 07/09/2026
Accepted: 10/09/2026
Online: 13/09/2026

**Keywords:**
Additive manufacturing,
Shell thickness,
Infill density,
Thermo-mechanical,
Fractography.

***Corresponding author:**
*jayasuteja@staff.ubaya.ac.id*

**Abstract**

The increasing demand for strong, lightweight, and thermally efficient battery casings in electric vehicles has accelerated the exploration of additive-manufactured sandwich structures. This research examined how shell thickness and infill density jointly affect the impact strength, mass, and thermal conductivity of sandwich-structured Polyethylene Terephthalate Glycol specimens produced via fused filament fabrication. A factorial experimental design was used, varying shell thickness (400, 800, and 1200 µm) and infill density (20, 50, and 80%). Two-way Analysis of Variance was applied to analyze the data statistically. The results revealed that shell thickness significantly influenced all three responses ($p \leq 0.05$), increasing impact strength by approximately 53% and thermal conductivity by approximately 31% as shell thickness increased from 400 to 1200 µm, at the cost of a nearly 35% increase in mass. Infill density strongly affected mass and thermal conductivity, increasing thermal conductivity by approximately 127% and mass by approximately 63% from 20% to 80% infill, but had a negligible effect on impact strength ($p > 0.05$). Then, fractography analysis revealed distinct failure modes and validated the meso-structure's role in mechanical and thermal performance. Applying desirability function-based multi-response optimization, the best configuration was determined to be a 1200 µm shell thickness paired with 50% infill density, predicting an impact strength of 28.57 kJ/m², thermal conductivity of 3.09 W/m·K, and mass of 3.34 g. This study provides a strategy for producing lightweight, impact-resistant, and thermally efficient additive-manufactured sandwich structures for potential electric vehicle battery casing applications.

## 1. Introduction

The growing demand for electric vehicles is driving demand for lightweight structures that increase energy efficiency and extend driving range to compete with internal combustion engines. Praveena *et al.* [1] proposed range-estimation strategies for long-distance EV travel but did not address structural mass reduction. Nicoletti *et al.* [2] quantified the lightweighting

potential of battery electric vehicles at the vehicle-system level, showing substantial efficiency gains, though without addressing component-level manufacturing strategies. Cheng *et al.* [3] reviewed continuous fiber-reinforced 3D-printed lightweight structures, highlighting their strength-to-weight advantages, but noted that process-property relationships for sandwich-type meso-structures remain insufficiently quantified. The use of lightweight structures for electric vehicle battery casings can also improve battery life and thermal stability [4]. In addition to being lightweight, battery casings must simultaneously ensure adequate mechanical strength and geometric adaptability to the aerodynamic design of electric vehicles [5].

Lithium-ion batteries and their derivatives, the most widely adopted in electric vehicles, operate safely within a narrow temperature range of –20 °C to 65 °C [6, 7]. Exceeding this range reduces performance and increases the risk of thermal runaway. Electric vehicle batteries consist of numerous battery cells enclosed within a battery casing [8]. Thus, battery casing structures must be designed not only to provide mechanical protection but also to facilitate effective heat transfer and temperature regulation.

Sandwich structures, composed of alternating skin and core layers as shown in Fig. 1, have emerged as promising candidates for lightweight, strong, and thermally-conductive battery casings.

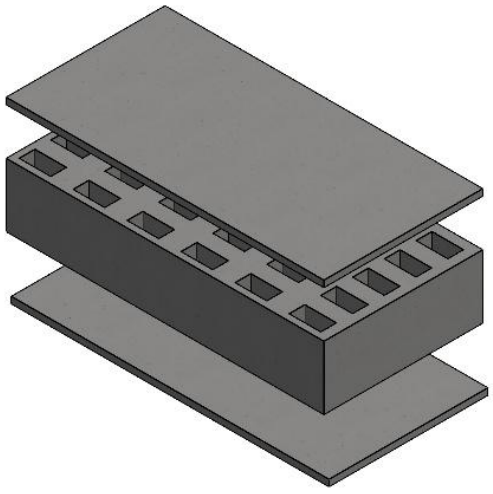


**Fig. 1.** Sandwich structure.

Wannarong and Singhanart reviewed 3D-printed honeycomb-core sandwich composites and reported favorable bending stiffness-to-weight ratios, but did not address thermal performance [9]. Bai *et al.* analyzed heat transfer in lattice-core sandwich panels, demonstrating enhanced conduction pathways, though their study was limited to numerical modeling without experimental validation [10]. Li *et al.* examined forced convection in folded-core sandwich structures, showing improved heat dissipation, but their configurations were not manufactured via additive processes suitable for complex battery-casing geometries [11]. Sandwich structures can also be strengthened by adding continuous fibers as fillers and strengtheners [3, 4]. With the advancement of 3D-printing technology, complex sandwich geometries can be additively manufactured with tailored infill architectures. Faidallah *et al.* [12] and Anwajler *et al.* [13] demonstrated that optimized internal lattice/cellular structures improve mechanical and thermal-insulation performance, respectively, but each study varied only a single structural parameter. Nordin *et al.* [14], Singh *et al.* [15], and Sonsalla *et al.* [16] investigated infill pattern and density effects on the thermal conductivity of ABS-based prints, consistently finding density-dependent conductivity. Still, none considered PETG or the combined role of shell thickness. Suteja and Soesanti [17] reviewed infill design parameters for PLA mechanical properties, concluding that infill pattern and density are the most studied variables, while shell/wall parameters remain comparatively underexplored — a gap this study directly addresses.

The process parameters of 3D-printing technology influence the geometry of sandwich structures. Previous studies have implemented 3D printing to create sandwich structures with different materials. However, safety protection for electric vehicle batteries can still be improved to meet consumer expectations [18].

Based on previous studies, the most investigated parameters in 3D printing are the infill pattern and infill density. The mechanical properties most frequently studied in previous studies are tensile, flexural, and compressive strength. The mechanical properties most

frequently studied in previous research are tensile, flexural, and compressive strength, though each study has typically examined only one of these in isolation. Wijayanto et al. focused on compressive strength, printing 24 PLA parts with 12 infill patterns at 50% density to identify the pattern giving the highest compressive strength with the shortest filament length, but did not assess tensile or flexural performance [19]. Dobos, Hanon, and Oldal centered on tensile strength and elastic modulus, using these to build a predictive model for the load capacity of PLA sandwich structures under bending, leaving compressive behavior unexamined [20]. Arifvianto et al. also emphasized tensile properties—tensile strength, strain at break, and elastic modulus—alongside hardness in PLA/TPU multi-material sandwiches, without testing compressive or flexural strength [21], while Yousefi Kanani and Kennedy concentrated on flexural strength, evaluating foamed PLA sandwich beams under three-point bending against analytical and numerical models, without addressing compressive strength or infill-pattern variation [22]. Thus, although tensile, flexural, and compressive strength dominate the literature, no study has combined all three properties within a single experimental framework that also accounts for infill pattern, density, and multi-material sandwich effects together. However, for battery casing applications, this study focuses on impact strength to help minimize collision damage [23]. The shell thickness and infill density simultaneously influence the impact strength and mass of sandwich structures, as the shell thickness determines the required infill density to achieve a specific mechanical strength and mass. In addition, the infill density and shell thickness affect the thermal conductivity of the sandwich structures. While previous studies have largely focused on the influence of infill pattern and density, few have addressed how shell thickness and infill density jointly optimize the thermo-mechanical performance of sandwich structures. This study aims to fill this gap by statistically quantifying the interaction of shell thickness and infill density, conducting a fracture analysis to evaluate the impact of shell thickness and infill density on the meso-structural behavior, and then optimizing the combined effects of shell thickness and infill density on the impact strength, mass, and thermal conductivity of sandwich structures.

The main innovation of this study is the development of an integrated experimental–statistical framework that, for the first time, jointly links the interaction effects of shell thickness and infill density to three simultaneous performance responses (impact strength, mass, and thermal conductivity) of 3D-printed sandwich structures, and resolves their inherent trade-offs through a desirability-based multi-response optimization validated by fractographic evidence. While parameter screening of 3D-printed sandwich structures has been reported in prior literature, this work advances the field by: (1) quantifying the statistical interaction effects between shell thickness and infill density on three simultaneous responses; (2) correlating macroscopic performance with microstructural fracture mechanisms specific to sandwich architectures; and (3) applying a desirability-based multi-response optimization framework to resolve conflicting lightweight, impact-resistant, and thermally-conductive objectives. These contributions provide novel design guidelines for multifunctional 3D-printed structures targeting EV battery casing applications.

## 2. Methodology

### *2.1. Materials and equipment*

The sandwich structures were fabricated using a Fused Filament Fabrication (FFF) 3D printer (Anycubic Kobra) with a 220 mm × 220 mm × 250 mm build volume. Ultimaker Cura software was utilized for model slicing, parameter setting, and printer operation. The sandwich structures were fabricated as single material objects in which the outer skin and internal core were printed continuously in one build using the FFF process, rather than as separately bonded skin and core layers. The skin was formed by concentric perimeter toolpaths deposited around the object boundary, with the number of perimeter passes determined by the target shell thickness divided by the nozzle diameter. The core region enclosed by the skin was filled using a specified infill pattern printed at a specified

infill angle and infill density. All objects were printed in the same orientation and under identical thermal conditions to isolate the effects of shell thickness and infill density from other process variables.

Two specimen types representing sandwich structures were designed as 3D stereolithography models. The first specimen is subjected to Charpy impact testing in accordance with ISO 179-1/1eU, and the second specimen is subjected to thermal conductivity analysis in accordance with ASTM C518-04. The unnotched specimen is used because it allows for a better assessment of the energy required for both crack initiation and subsequent propagation, rather than just the stress concentration at a machined notch. Fig. 2 and Fig. 3 illustrate the Charpy impact test and thermal conductivity test specimens, respectively, along with their dimensions.

The material employed in this study was Polyethylene Terephthalate Glycol (PETG). This selection is based on its thermomechanical properties, which are suitable for battery casing applications. Compared with the commonly used Polylactic Acid, PETG offers a superior combination of properties, including better mechanical strength, higher thermal conductivity, and lower density [24]. These characteristics are crucial for ensuring structural integrity and effective thermal management of the casings.

Furthermore, PETG has a glass transition temperature ($T_g$) and a melting temperature (Tm) that exceed the battery's targeted operating temperature range. This thermal stability ensures that the casings' structural and dimensional integrity are maintained without heat deflection during normal operation, making it a viable candidate for this application. The PETG filament used in this study was manufactured by SUNLU (Zhuhai Sunlu Industrial Co., Ltd., Zhuhai, China).

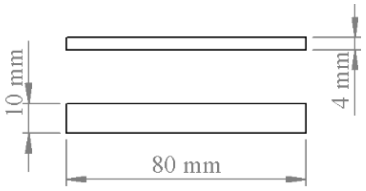



**Fig. 2.** Impact test specimen.

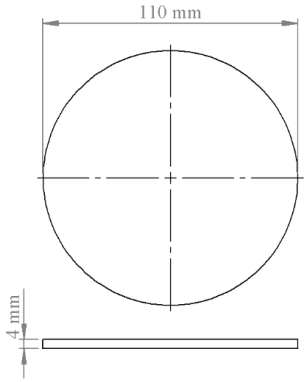



**Fig. 3.** Thermal conductivity test specimen.

### *2.2. Research method*

This study employed a Factorial Design with two replications to obtain sufficiently dependable data without expending excessive resources. A full factorial design was selected because it enables the main effects of shell thickness and infill density, as well as their two-way interaction effect, to be estimated and tested for statistical significance, which a one-factor-at-a-time approach cannot capture. Two replications per treatment combination were included to provide a pooled estimate of experimental error while keeping the total number of specimens within a practical and resource-efficient range.

Two FFF-printing parameters were investigated as the independent factors: shell thickness and infill density, selected based on a literature review and printer catalogs. Shell thickness and infill density were selected as the investigated input parameters because prior literature identifies them as the two meso-structural parameters with the greatest influence on the mechanical and thermal performance of sandwich-type FFF parts. Yet, their combined/interactive effect on multiple simultaneous responses remains insufficiently characterized.

The levels of these parameters are shown in Table 1. The shell thickness levels were selected as multiples of the 400 µm nozzle diameter, representing the practical range achievable without excessive print time or material waste. The infill density levels were selected to span low, moderate, and high-density regimes commonly investigated in the FFF literature for structural applications.

All remaining printing parameters were held constant and controlled in accordance with the literature, manufacturer specifications, and software recommendations, as summarized in Table 2. For example, the Line infill pattern used in this study was adopted from a previous study [25]. The response variables measured in this experiment were the impact strength, mass, and thermal conductivity of the printed specimens.

The printing sequence for all test specimens was randomized to mitigate systematic bias. The study employed a 3 × 3 factorial design with two replications, resulting in a total of eighteen specimens being printed for each test type. For each of the nine factor-level combinations, two replicate specimens were printed and tested (n = 2 readings per condition), yielding 18 individual readings per response variable, consistent with the total of eighteen specimens described above. The Charpy impact strength was measured for the impact specimens in accordance with ISO 179-1/1eU.

Simultaneously, the thermal conductivity of the corresponding specimens was measured in accordance with ASTM C518-04. The dimensions of each specimen were measured with callipers, and its mass with a precision balance.

Analysis of Variance (ANOVA) was performed at a 95% confidence level ($\alpha = 0.05$). Therefore, parameters with p-values $\leq 0.05$ were considered to have a statistically significant effect on the corresponding response.

**Table 1.** Investigated parameters.

| Parameter | Value |
|---|---|
| Shell thickness (μm) | 400, 800, 1200 |
| Infill density (%) | 20, 50, 80 |

**Table 2.** Controlled parameters.

| Parameter | Value |
|---|---|
| Nozzle diameter (μm) | 400 |
| Layer height (μm) | 200 |
| Infill pattern | Line |
| Infill angle (°) | 0 |
| Printing temperature (°C) | 240 |
| Bed temperature (°C) | 80 |
| Printing speed (mm/sec) | 60 |
| Printing orientation | On-edge |

For the analysis, only the mass of the impact test specimens was considered, as it is directly correlated with the mass of the thermally-conductive specimens printed under identical printing conditions.

A fracture analysis was subsequently conducted to understand the influence of shell thickness and infill density on the impact strength, mass, and thermal conductivity of the specimens. Fracture analysis was performed on the specimens exhibiting the lowest and highest impact strength using the AmScope MU1403 optical microscope at multiple magnifications, examining both the fracture surface perpendicular to the impact direction and the cross-section along the specimen thickness, to identify the dominant failure mode and relate it to the shell/infill meso-structure. Next, a multi-response optimization framework was employed to concurrently optimize impact strength, thermal conductivity, and mass of the sandwich structures.

## 3. Results and discussion

### *3.1. Experimental data*

Figs. 4 and 5 show printed specimens for impact strength and thermal conductivity, respectively. Table 3 compiles the related experimental data for all specimens in run order. The general factorial regression model demonstrated a strong and statistically significant fit to the data, with a minimum coefficient of determination $R^2$ of 0.94. This high $R^2$ value indicates that at least 94% of the variance in the dependent variable is explained by the independent variables included in the model.



**Fig. 4.** Impact test specimen.



**Fig. 5.** Thermal conductivity test specimen.

**Table 3.** Experimental data.

| Run Order | Shell thickness (μm) | Infill density (%) | Impact strength (kJ/m$^2$) | Mass (gr) | Thermal conductivity (W/m·K) |
|---|---|---|---|---|---|
| 1 | 400 | 20 | 14.207 | 2.01 | 1.268 |
| 2 | 1200 | 20 | 23.811 | 2.94 | 2.138 |
| 3 | 400 | 20 | 15.103 | 2.03 | 1.294 |
| 4 | 1200 | 80 | 24.756 | 3.57 | 4.450 |
| 5 | 400 | 80 | 19.696 | 3.56 | 3.736 |
| 6 | 1200 | 80 | 24.700 | 3.52 | 4.279 |
| 7 | 800 | 20 | 24.202 | 2.50 | 1.739 |
| 8 | 800 | 80 | 24.744 | 3.60 | 3.843 |
| 9 | 400 | 50 | 15.126 | 2.81 | 2.286 |
| 10 | 400 | 50 | 17.321 | 2.80 | 2.532 |
| 11 | 1200 | 50 | 29.653 | 3.34 | 3.339 |
| 12 | 1200 | 20 | 27.792 | 2.97 | 1.688 |
| 13 | 800 | 50 | 23.005 | 3.05 | 2.558 |
| 14 | 800 | 50 | 20.940 | 3.04 | 2.278 |
| 15 | 800 | 80 | 24.692 | 3.59 | 2.873 |
| 16 | 400 | 80 | 22.055 | 3.56 | 3.160 |
| 17 | 1200 | 50 | 27.496 | 3.34 | 2.848 |
| 18 | 800 | 20 | 22.617 | 2.51 | 1.734 |

The ANOVA results, shown in Table 4, revealed that shell thickness is the dominant factor influencing the response, contributing 75.43% of the total variation (F = 60.61, P = 0.000). At the same time, its interaction with infill density adds a further significant contribution of 14.92% (P = 0.012). This indicates that infill density's effect depends on the shell thickness setting. Infill density alone accounts for only 4.06% and is not statistically significant (P = 0.086), suggesting its influence is primarily expressed through this interaction rather than independently. With the Error term accounting for just 5.60%, the model explains 94.40% of the total variability, demonstrating a strong overall fit. On the other hand, all investigated factors had a significant effect on both the specimen mass and the thermal conductivity, as shown in Tables 5 and 6.

For the mass response, the ANOVA results show that the model explains 100% of the total variation, with an error of only 0.04%. Infill density emerges as the dominant factor contributing 74.8% to the variation in mass (F = 9147.41, P = 0.000), followed by shell thickness at 15.2%. The interaction between shell thickness and infill density contributed 10% (P = 0.000), indicating that the effect of one factor depends on the level of the other. This dominance of infill density over shell thickness makes physical sense for a mass response, since infill density directly determines the amount of material deposited inside the part. In contrast, shell thickness primarily governs the outer wall volume.

For the thermal conductivity response, the ANOVA results indicate that the model explains 94.2% of the total variation with a reasonably good fit (error of 5.8%). Infill density again emerges as the dominant factor, contributing 80.1 % to the variation in thermal conductivity (F = 62.00, P = 0.000), followed by shell thickness at 11.8% (P = 0.007), though with a much smaller contribution. The interaction between shell thickness and infill density accounts for only 2.3% and is not statistically significant (P = 0.504 > 0.05), indicating that the two factors act independently and additively on thermal conductivity rather than interacting with one another.

**Table 4.** Analysis of variance in impact strength.

| Source | DF | Adj SS | F-value | P-value | PCR (%) |
|---|---|---|---|---|---|
| Model | 8 | 324216086 | 18.96 | 0.000 | 94.4 |
| Linear | 4 | 272990390 | 31.94 | 0.000 | 79.5 |
| Shell thickness | 2 | 259054272 | 60.61 | 0.000 | 75.4 |
| Infill density | 2 | 13936118 | 3.26 | 0.086 | 4.1 |
| 2-way interactions | 4 | 51225696 | 5.99 | 0.012 | 15 |
| Shell thickness * Infill density | 4 | 51225696 | 5.99 | 0.012 | 15 |
| Error | 9 | 19232967 | | | 5.6 |
| Total | 17 | 343449053 | | | 100 |

**Table 5.** Analysis of variance in mass.

| Source | DF | Adj SS | F-value | P-value | PCR (%) |
|---|---|---|---|---|---|
| Model | 8 | 4.629 | 3055.97 | 0.00 | 100 |
| Linear | 4 | 4.167 | 5502.15 | 0.00 | 90.0 |
| Shell thickness | 2 | 0.703 | 1856.89 | 0.00 | 15.2 |
| Infill density | 2 | 3.464 | 9147.41 | 0.00 | 74.8 |
| 2-way interactions | 4 | 0.462 | 609.78 | 0.00 | 10 |
| Shell thickness * Infill density | 4 | 0.462 | 609.78 | 0.00 | 10 |
| Error | 9 | 0.002 | | | 0 |
| Total | 17 | 4.630 | | | 100 |

**Table 6.** Analysis of variance in thermal conductivity.

| Source | DF | Adj SS | F-value | P-value | PCR (%) |
|---|---|---|---|---|---|
| Model | 8 | 15.268 | 18.23 | 0.000 | 94.2 |
| Linear | 4 | 14.891 | 35.55 | 0.000 | 91.9 |
| Shell thickness | 2 | 1.907 | 9.10 | 0.007 | 11.8 |
| Infill density | 2 | 12.985 | 62.00 | 0.000 | 80.1 |
| 2-way interactions | 4 | 0.376 | 0.90 | 0.504 | 2.3 |
| Shell thickness * Infill density | 4 | 0.376 | 0.90 | 0.504 | 2.3 |
| Error | 9 | 0.942 | | | 5.8 |
| Total | 17 | 16.210 | | | 100 |

This pattern is consistent with the physical role of infill density in governing the internal air-to-material ratio, which directly controls heat conduction pathways within the printed part. In contrast, shell thickness has a comparatively minor and largely independent effect.

### *3.2. Impact strength*

The main effects and standard deviation plots shown in Fig. 6 illustrate the influence of shell thickness and infill density on the mean impact strength of the printed specimens.

The analysis reveals that shell thickness is the dominant factor affecting impact strength. The plot shows that the mean impact strength increases substantially as the shell thickness increases from 400 µm to 1200 µm. This trend aligns with the expected mechanical behavior, as thicker shells can absorb and distribute greater impact energy, thereby inhibiting crack initiation and propagation [26].

In contrast, infill density has a statistically nonsignificant effect on impact strength over the tested range.

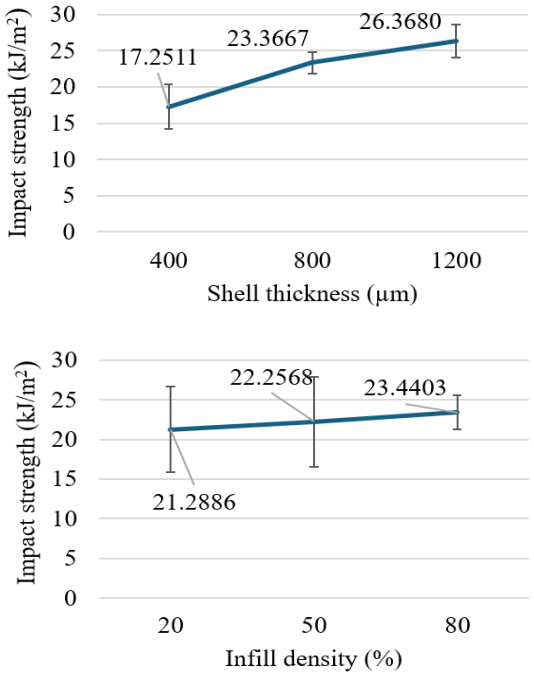



**Fig. 6.** Main effect and standard deviation plots of the impact strength.

The plot shows only slight fluctuations across the different infill levels (20 %, 50 %, 80 %). Compared to shell thickness, infill density contributes minimally to the impact resistance of these sandwich structures. This is primarily attributed to the Line infill pattern being oriented perpendicular to the shell. This specific geometric configuration and printing direction ensure that the impact load is uniformly distributed along the linear paths, rendering the overall impact performance largely independent of internal density [27].

At the lowest shell thickness, the impact strength is not stable, as indicated by the higher standard deviation. The large variation observed in thinner shells is attributed to the strong influence of infill density. In contrast, the error bars corresponding to different infill densities are relatively similar and moderate in length, except for the highest infill density.

This suggests that infill density exerts a more moderate influence on impact strength than shell thickness. Since the standard deviations are decreasing at the highest infill density levels, this level can be considered stable. The small variation observed in this infill density level indicates that the shell thickness does not

have a significant effect at high-level infill density.

The interaction plot presented in Fig. 7 shows the combined effect of shell thickness and infill density on the mean impact strength of the sandwich-structured specimens. This graphical representation indicates a statistically significant interaction effect between the two design parameters. The statistical test in Table 4 confirms this observation, with a p-value < 0.05, indicating a statistically significant effect.

As illustrated in Fig. 7, the mean impact strength strongly depends on both the shell thickness and infill density. The trajectories of the three infill density levels are distinctly non-parallel. This confirms that the effectiveness of increasing shell thickness in improving impact strength is dependent on the infill density.

At a 20% infill density, impact strength increased sharply as shell thickness increased from 400 to 800 µm. This suggests that for low-density internal structures, the outer shell plays a dominant role in absorbing impact energy. In contrast, at 80% infill density, although the initial strength at 400 m is already high, further shell thickening contributes minimally to impact resistance.

This behavior implies that the internal structure provides sufficient load-bearing capacity and reduces the influence of shell thickness at high infill densities. Compared with specimens printed at other infill densities, the specimens printed at 50% infill density exhibit a steeper gradient in impact energy absorption.

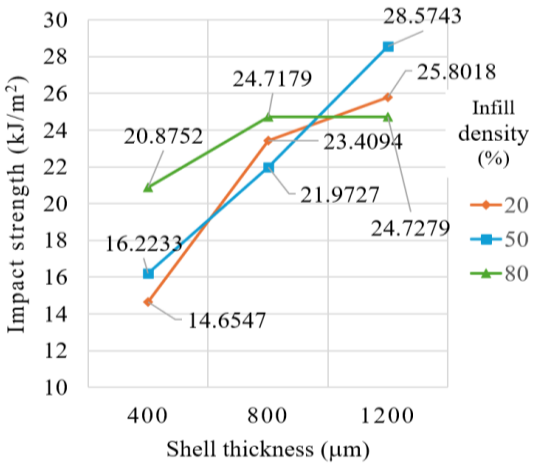



**Fig. 7.** Interaction plots of the impact strength.

An increase in the mean impact strengths indicates a strong synergistic effect between moderate infill density and a thicker shell. This combination seems to be the best for balancing material savings and mechanical strength.

Fracture analysis was performed on two representative specimens exhibiting the lowest and highest impact strengths, respectively. The specimen with the lowest impact strength was fabricated with a shell thickness of 400 µm and an infill density of 20%. Fig. 8 presents the fracture surface morphology of this specimen.

Fig. 8(a) displays the fracture surface perpendicular to the impact loading direction, while Fig. 8(b) illustrates the fracture along the specimen thickness.

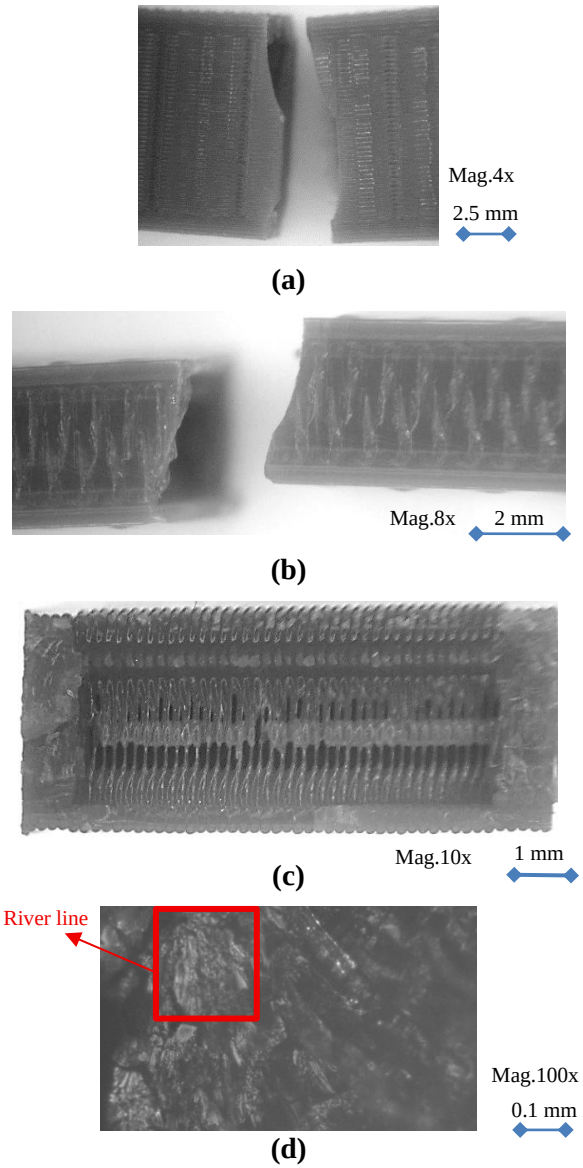



**Fig. 8.** Fracture surface morphology of the lowest impact strength specimen.

Both views reveal relatively flat, featureless fracture surfaces along the perimeter, with no evidence of fiber pull-out or ductile tearing, indicating limited energy-dissipation capacity.

Cross-sectional examination shown in Fig. 8(c) further confirms a smooth and planar fracture profile. The fracture was observed to occur at the shell and the infill, which provided negligible resistance to the applied force. High-magnification imaging of the cross-section, as shown in Fig. 8(d), reveals characteristic river-line patterns and indicates a rapid crack propagation typical of brittle fracture. The absence of plastic deformation features corroborates the brittle nature of the failure mode and is consistent with the observed low impact strength.

The highest impact strength was achieved by using a shell thickness of 1200 µm and an infill density of 50%. The corresponding fracture morphology is presented in Fig. 9. Figs. 9(a) and 9(b) reveal a highly irregular and fibrous fracture surface and indicate the significant energy dissipation during failure.

The cross-sectional fracture profile shown in Fig. 9(c) exhibits a rough and uneven topography that supports a non-brittle failure mechanism. The observed failure in the infill indicates that it also helped resist the applied force. High-magnification imaging of the cross-section, as depicted in Fig. 9(d), shows a complex surface morphology characterized by both ductile features, such as microvoid coalescence and localized river-line patterns, that are typically associated with brittle fracture. Fig. 9(c) and (d) suggest the presence of plastic deformation zones, which may be attributed to improved interlayer diffusion and load transfer in thicker shell configurations. This mixed-mode failure behavior suggests a combination of ductile and brittle characteristics, thereby contributing to the specimen's increased impact strength. The observed increase in impact strength with greater shell thickness can be attributed to the improved load-bearing capacity of the outer wall, which effectively constrains crack propagation and mitigates interlayer delamination. This phenomenon is well-aligned with established principles of fracture mechanics.

While the observed fracture features provide visual evidence, the mechanistic interpretation suggests that the transition from brittle to mixed-mode failure is likely governed by the constraint effect of the thicker shell on crack propagation paths. The presence of microvoid coalescence in high-strength specimens may be attributed to enhanced diffusion of polymer chains across layer interfaces during extended residence in the molten state. However, it should be noted that the non-significant effect of infill density on impact strength may also be due to the specific line infill topology used, which distributes stress differently than other patterns.

The experimental data were also compared with findings from previously published studies. The observed increase in impact strength with increasing infill density is consistent with the results reported by Banić *et al*. [28]. This agreement can be explained by the fact that increasing infill density reduces internal voids and improves interlayer adhesion, thereby enhancing a material's ability to absorb and dissipate impact energy. As a result, parts with denser infill exhibit improved fracture resistance under dynamic loading.

In contrast, the current study's observation that increasing shell thickness increases impact strength does not align with the findings of Hamzah *et al.* [29]. The discrepancy can be attributed to differences in the shell parameters used. Specifically, Hamzah *et al.* used a significantly larger number of shells and thicker shells than in this study. Excessive shell thickness increases the rigidity of the printed structure, reducing its capacity for plastic deformation during impact and, consequently, making the material more brittle. This interpretation is supported by Mazlan *et al.* [30], who reported that an excessive number and size of shells result in printed parts with higher stiffness but lower toughness, ultimately reducing impact resistance.

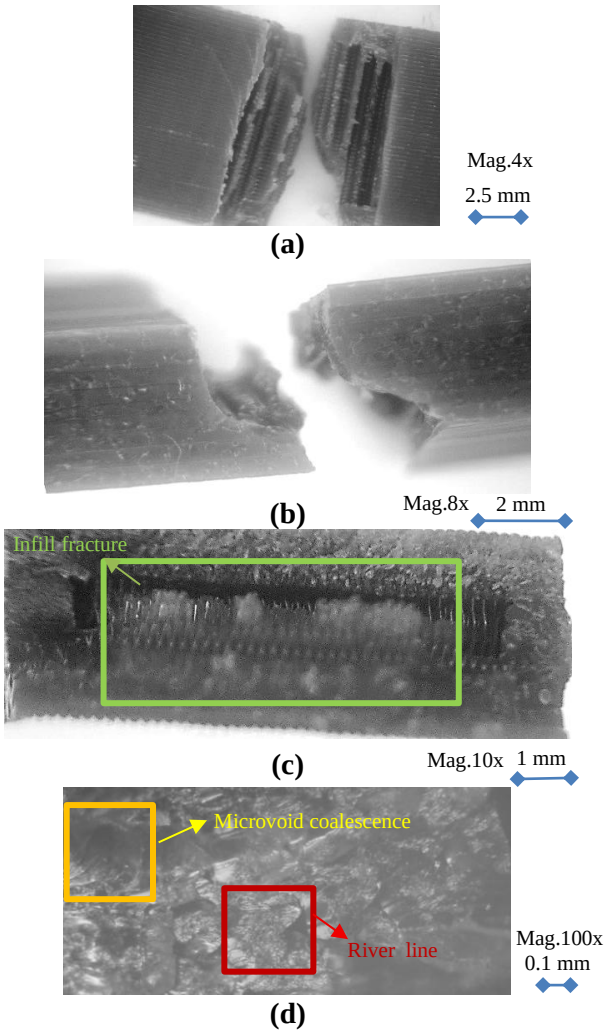



**Fig. 9.** Fracture surface morphology of the highest impact strength specimen.

### *3.3. Mass*

Fig. 10 shows the individual effects of shell thickness and infill density on the mean mass of the printed impact specimens, including their standard deviation. The plot shows that both shell thickness and infill density have significant and positive effects on specimen mass. As the shell thickness increases from 400 µm to 1200 µm, the mean mass tends to increase. This is a consequence of the increased volume of material deposited to form the structure's solid outer walls. Similarly, a positive relationship is observed for the infill density. Increasing the infill percentage from 20% to 80% increased the mean mass. This trend is expected, as a higher infill density deposits more material within the structure's internal core during printing. The standard deviation distributions in both figures indicate the consistency of the measured mass across printing parameters.

For shell thickness variation, the error bars show moderate deviations that slightly decrease as the shell thickness increases. This reduction in standard deviation implies that the influence of infill density decreases at higher shell thicknesses, likely because a substantial increase in wall volume becomes a more significant contributor to the added mass than an increase in infill density [31].

Meanwhile, the error bars for different infill densities decrease in length, suggesting that shell thickness has less influence at higher infill density. The near-zero standard deviation at the highest infill density indicates that the effect of shell thickness on mass is small. This uniformity also demonstrates that the infill already accounts for almost all of the object's volume and mass.

The interaction plot shown in Fig. 11 demonstrates that a significant interaction between shell thickness and infill density governs the mass of the sandwich-structured specimens. As shown in Table 5, the observation is supported by a p-value below 0.05, indicating a statistically significant effect.

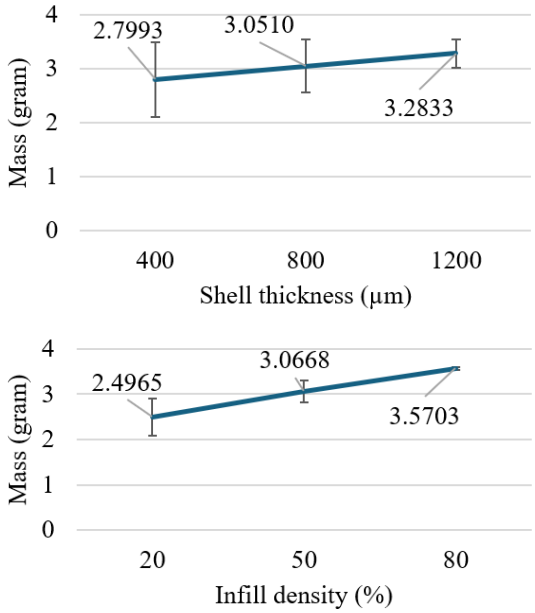



**Fig. 10.** Main effect and standard deviation plots of the mass.

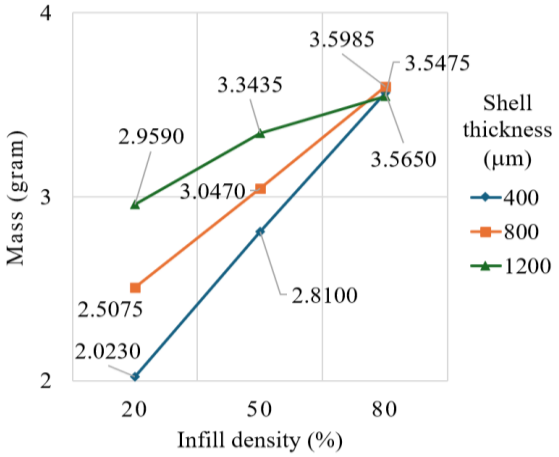



**Fig. 11.** Interaction plots of the mass.

The nonparallel trends across shell thickness levels confirm that the effect of infill density on mass is not independent but is controlled by the outer shell's geometric contribution.

At low shell thickness, the specimen mass increases sharply with infill density. This indicates that the internal material volume dominates mass accumulation when the shell is thin. Conversely, mass increases more gradually at high shell thicknesses, indicating that the shell thickness contributes substantially to the total mass and reduces the relative impact of infill density variation.

### *3.4. Thermal conductivity*

The main effects and standard deviation plot shown in Fig. 12 exhibits the individual effects of shell thickness and infill density on the thermal conductivity of the printed specimens. The analysis reveals that both parameters have a significant positive influence on thermal conductivity. For shell thickness, a substantial increase in mean thermal conductivity is observed as the thickness increases from 400 µm to 1200 µm. This trend is attributed to the greater cross-sectional area of the solid shell, which enables greater heat conduction than the porous internal structure.

Similarly, a strong positive effect is observed for the infill density. Increasing the infill from 20% to 80% increases the thermal conductivity. This is a consequence of reducing the void fraction within the core of the sandwich structures. A higher infill density reduces the amount of entrapped air, which is a poor thermal conductor, and replaces it with a polymer material [32]. As a result, the overall heat transfer capability through the solid phase increases.

For variations in shell thickness, the error bars exhibit relatively large deviations, particularly at the lowest and highest thickness levels. This fluctuation suggests that the heat transfer behavior is more sensitive to structural differences within the printed walls. The higher standard deviations may be linked to infill density, as differences in internal structure affect the uniformity of heat conduction.

In contrast, the error bars corresponding to infill density are shorter and more consistent across all density levels. The reduced standard deviation indicates that infill density affects void-induced thermal resistance and thermal transport measurements more than shell thickness does. Overall, the error bar patterns indicate that shell thickness introduces greater variability, whereas infill density yields more consistent and controllable effects on thermal conductivity.

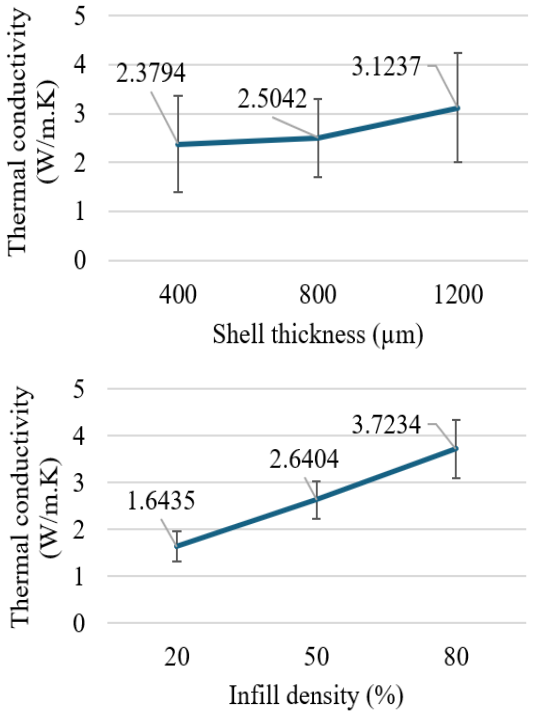



**Fig. 12.** Main effect and standard deviation plots of the thermal conductivity.

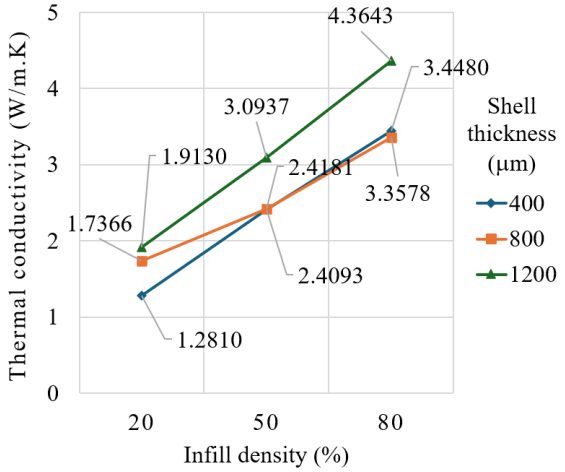



**Fig. 13.** Interaction plots of the thermal conductivity.

Fig. 13 reveals the interaction effect between the shell thickness and infill density on the mean thermal conductivity of the sandwich-structured specimens. The influence of infill density on thermal performance varies depending on the structural contribution of the outer shell. The nonparallel trends across different shell thicknesses confirm this relationship.

At low infill density, increasing the shell thickness contributes only marginally to the overall thermal conductivity because the highly porous internal structure constrains heat-conduction paths within the voids. At moderate infill density, increasing shell thickness initially shows no effect, then transitions to an increase in the maximum shell thickness.

A reasonable explanation is that a thicker shell establishes structures that provide a pathway for conduction heat transfer. At high infill density, while the internal structure is sufficiently dense, an increase in shell thickness results in higher conductivity. This implies that thick shells amplify the thermal benefit of dense infill by providing a continuous, low-thermal-resistance conduction path.

To further interpret these trends, at the microstructural level, variations in shell thickness strongly influence the interlayer density. Thicker shells exhibit enhanced interlayer fusion and reduced interfacial porosity due to longer residence times in the molten state during deposition. This condition minimizes interfacial resistance arising from air gaps between layers and promotes better continuity of thermal conduction pathways within the printed sandwich structures.

Conversely, thinner shells tend to cool rapidly, resulting in discrete layer interfaces and microvoids. Discrete layer interfaces were observed on the surface of the specimen, with the lowest shell thicknesses shown in Fig. 14. These voids decrease the effective contact area between extrudate strands. As a result, specimens with thinner shells exhibit lower effective thermal conductivity compared to their thicker counterparts.

An increase in the thermal conductivity with increasing infill density was also reported by Lopes *et al.* [33]. These findings are consistent with the work of Khanafer *et al.* [34]. The improvement is generally attributed to reduced internal porosity, the formation of denser heat-transfer pathways, and a diminished presence of air gaps, which act as thermal insulators. However, Ahmad *et al.* reported the opposite results, showing that a reduction in shell thickness led to improved thermal conductivity [35].

This discrepancy may be attributed to the significant contact resistance between the shells in their study, where poor interfacial bonding or incomplete fusion between adjacent layers increased the thermal barrier. Under ideal conditions, increasing the shell thickness can enhance thermal conductivity, particularly when intershell bonding is strong, surfaces are smooth, and porosity is low. However, greater shell thickness may act as a thermal barrier due to conduction resistance in the material and fluid-flow considerations, suggesting an optimal shell thickness.

The elevated thermal conductivity values reported in this study do not reflect the intrinsic properties of bulk PETG. Rather, these values reflect the effective thermal conductivity of an optimized 3D-printed sandwich structure.

Sandwich structures featuring thick shells and dense infill create more efficient parallel conduction pathways compared to homogeneous bulk material, resulting in effective values that can significantly exceed those reported for bulk PETG in the literature [33]. Measurements conducted in accordance with ASTM C518-04 quantify steady-state heat transfer through the

specimen thickness, including contributions from the solid shell, infill structure, and interlayer interfaces.

The combination of increased shell thickness and high infill density establishes more continuous heat-conduction pathways through the specimen thickness. Enhanced interlayer fusion reduces interfacial porosity and minimizes discrete layer interfaces observed in Fig. 14, thereby improving the continuity of heat conduction pathways through the specimen thickness. Furthermore, the selected printing orientation, infill pattern, and infill angle parameters result in printed specimens with the measured heat-transfer direction parallel to the filament-extrusion direction. This configuration ensures that heat conduction pathways do not need to traverse numerous high-resistance inter-layer interfaces. Instead, the thermal load is evenly distributed among the directly connected filaments.

In addition to conduction through the solid PETG, natural convection within the air voids of the infill structure also contributes to the increase in measured effective thermal conductivity. In the investigated specimens, the remaining air voids form interconnected internal channels. When a temperature gradient exists through the specimen thickness, the warmer air within the voids becomes less dense and rises, generating convection currents that transfer heat from the hot side to the cold side. This aligns with findings by Zorzetto Bittencourt *et al.,* who demonstrated that the effective thermal conductivity of porous 3D-printed structures is influenced by natural convection [36].

Overall, the findings demonstrate that shell thickness plays a dominant role in balancing the mechanical and thermal performance of PETG-based 3D-printed sandwich structures. Meanwhile, infill density primarily governs mass and thermal conductivity. These results emphasize the necessity of parameter optimization tailored to both the material properties and functional requirements of the battery casings. The nonsignificant effect of infill density on impact strength in this study needs further discussion.

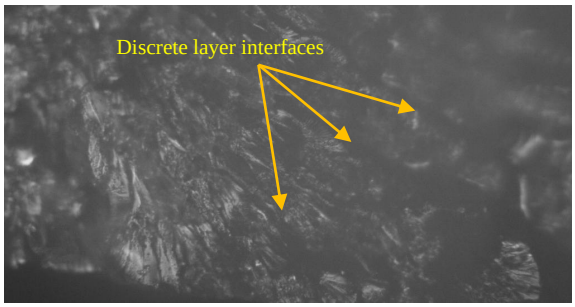



**Fig. 14.** Discrete layer interfaces.

While higher density generally improves structural stiffness, the line infill pattern employed here minimized the influence of density by ensuring consistent load transfer across shell boundaries. This finding suggests that the mechanical contribution of infill density is highly dependent on the infill pattern. This highlights the importance of considering not only density levels but also the infill topology when designing sandwich structures for multifunctional applications.

### *3.5. Optimization*

This study has established a statistically driven framework to predict the interactions between shell thickness and infill density on the impact strength, thermal conductivity, and overall mass of sandwich-structured specimens produced via fused filament fabrication. To resolve the conflicting objectives, a multi-response optimization framework based on the Desirability Function Approach was employed. This method converted each predicted response (impact strength, mass, and thermal conductivity) into a dimensionless individual desirability value di ranging from 0 (completely undesirable) to 1 (fully desirable), based on the regression models obtained from the factorial ANOVA. The individual desirabilities were then aggregated into a single composite desirability index using the geometric mean. The parameter combination (shell thickness and infill density) that maximizes the composite desirability index over the continuous design space was then identified as the optimal compromise solution.

All responses were assigned equal importance, reflecting a balanced design philosophy that prioritizes none over the others. Equal weighting

provides a balanced, unbiased compromise solution that does not arbitrarily favor one objective over another.

The predictive model identifies an optimal configuration for maximum impact strength at a shell thickness of 1200 μm and an infill density of 50%, yielding a predicted strength of 28.5743 kJ/m$^2$ and a high desirability index (D = 0.9302). Maximizing thermal conductivity is achieved with a shell thickness of 1200 μm and an infill density of 80%, resulting in a predicted value of 4.3643 W/m·K and a near-ideal desirability (D = 0.9732). To minimize mass, the optimization converges to a shell thickness of 400 μm and an infill density of 20%, yielding a predicted mass of 2.0230 grams with an exceptional desirability (D = 0.9997). However, these individual optima are mutually exclusive, underscoring the need for a compromise solution.

A desirability-based multi-response optimization was therefore conducted to aggregate individual desirabilities into a composite objective function. The resulting global optimum, with a shell thickness of 1200 μm and a 50% infill density, represents a trade-off that balances all three objectives with equal weighting. At this setting, the predicted responses are an impact strength of 28.5743 kJ/m$^2$ with a desirability of 0.9302, a thermal conductivity of 3.0937 W/m·K with a desirability of 0.5739, and a mass of 3.3435 grams with a desirability of 0.1627.

The overall composite desirability shows that impact strength remains near its individual optimum, while thermal conductivity remains acceptable, and the substantial gains in mechanical and thermal performance justify mass. Although the low desirability for mass reflects the inherent conflict between impact strength and weight, this configuration outperforms the typical 3D-printed benchmark in impact strength performance [37-41].

These findings enable the fabrication of sandwich structures that are sufficiently lightweight, mechanically resilient under impact loading, and capable of dissipating moderate heat. The reported optimum represents a model-predicted solution. An experimental confirmation at this exact parameter set is recommended for application-critical implementations. These results offer guidelines for designers to balance structural integrity, thermal management, and material efficiency in 3D-printed sandwich structures.

## 4. Conclusions

This study investigated the effects of shell thickness (400, 800, and 1200 μm) and infill density (20, 50, and 80%) on the impact strength, mass, and thermal conductivity of FFF-printed PETG sandwich structures intended for electric vehicle battery casing applications. Eighteen specimens per test type were fabricated according to a 3 × 3 factorial design with two replications, tested in accordance with ISO 179-1/1eU and ASTM C518-04, and analyzed using two-way ANOVA. Fractographic analysis was subsequently performed to relate the responses to meso-structural failure mechanisms, and a desirability-based multi-response optimization was applied to identify the parameter combination that best balances the three, partly conflicting, objectives.

The main findings of this study are summarized as follows:

1. Shell thickness had a statistically significant effect on all three responses, whereas infill density significantly affected mass and thermal conductivity but had a non-significant effect on impact strength.
2. Increasing shell thickness from 400 μm to 1200 μm increased impact strength by approximately 53% and thermal conductivity by approximately 31%, at the cost of a nearly 35% increase in mass.
3. Increasing infill density from 20% to 80% increased thermal conductivity by approximately 127 % and impact strength by approximately 10%, while increasing mass by approximately 63%.
4. The negligible effect of infill density on impact strength is attributed to the uniform stress distribution provided by the Line infill pattern, indicating that the mechanical contribution of infill density is strongly dependent on infill topology.
5. Fractography confirmed that specimens with thin shells and low infill density failed in a brittle, low-energy-absorption mode. In

contrast, specimens with thick shells and moderate infill density exhibited mixed ductile–brittle fracture with greater energy dissipation, consistent with their higher measured impact strength.

6. Desirability-based multi-response optimization identified a shell thickness of 1200 µm and an infill density of 50% as the best overall compromise, yielding a predicted impact strength of 28.5743 kJ/m², thermal conductivity of 3.0937 W/m·K, and mass of 3.3435 g.

This work provides, to our knowledge, the first statistically quantified interaction analysis between shell thickness and infill density across three simultaneous thermo-mechanical responses for FFF-printed PETG sandwich structures, links these responses to meso-structural fracture mechanisms via fractography, and delivers an experimentally validated, desirability-based optimization framework offering practical design guidelines for producing lightweight, impact-resistant, and thermally efficient PETG sandwich structures via fused filament fabrication.

A limitation of this work is that the optimized compromise solution was derived solely through statistical modeling and the Desirability Function Approach without physical validation. Nevertheless, this study provides a robust theoretical foundation for multi-response optimization in additive manufacturing, and physical testing will be executed in the next phase of this research to confirm the model's real-world accuracy. The findings are based on standardized material-level tests using a single infill pattern, a single material, and a limited parameter range. System-level mechanical loading, full battery-pack thermal management behavior, and compliance with automotive standards such as UNECE R100 were not evaluated. Future work will extend this framework to alternative infill patterns and multi-material sandwich configurations, scale the optimized configuration to prototype-level battery casing geometries, and integrate the results with multiphysics simulations and system-level compliance testing to support industrial implementation.

**Acknowledgment**

This work was supported by the Ministry of Higher Education, Science, and Technology, Republic of Indonesia, through the Fundamental Research Grant Scheme (128/C3/DT.05.00/PL/2025). The authors would like to express their sincere gratitude for the financial support.

**References**

[1] M. Praveena, R. Mohan Kumar and Y. Manoj, "Range estimation and optimization techniques for electric vehicle long-distance travel" *Proc. 7th Int. Conf. Electron. Commun. Aerosp. Technol.*, pp. 241–246, (2023).

[2] L. Nicoletti, A. Romano, A. König, P. Köhler, M. Heinrich and M. Lienkamp, "An estimation of the lightweight potential of battery electric vehicles" *Energies*, Vol. 14, No. 15, pp. 1–29, (2021).

[3] P. Cheng *et al.*, "3D printed continuous fiber reinforced composite lightweight structures: A review and outlook" *Compos. Part B Eng.*, Vol. 250, No. July 2022, p. 110450, (2023).

[4] Y. An, X. Wang, N. Dou and Z. Wu, "Strength analysis of the lightweight-designed power battery boxes in electric vehicle" *E3S Web Conf.*, Vol. 341, p. 01025, (2022).

[5] X. Chen, J. Wang, K. Zhao and L. Yang, "Electric vehicles body frame structure design method: An approach to design electric vehicle body structure based on battery arrangement" *Proc. Inst. Mech. Eng. Part D J. Automob. Eng.*, Vol. 236, No. 9, pp. 2025–2042, (2021).

[6] S. Ma *et al.*, "Temperature effect and thermal impact in lithium-ion batteries: A review" *Prog. Nat. Sci. Mater. Int.*, Vol. 28, No. 6, pp. 653–666, (2018).

[7] M. F. I. M. Razi, Z. H. C. Daud, Z. Asus, I. I. Mazali, M. I. Ardani and M. K. A. Hamid, "A Review of internal resistance and temperature relationship, state of health and thermal runaway for lithium-

ion battery beyond normal operating condition" *J. Adv. Res. Fluid Mech. Therm. Sci.*, Vol. 88, No. 2, pp. 123–132, (2021).
[8] G. Kulkarni, "Comparative Material Selection of battery pack casing for an electric vehicle" *Int. J. Res. Appl. Sci. Eng. Technol.*, Vol. 11, No. 12, pp. 66–75, (2023).
[9] D. Wannarong and T. Singhanart, "A Review of sandwich composite structures with 3D printed honeycomb cores" *Eng. J.*, Vol. 26, No. 6, pp. 27–39, (2022).
[10] X. Bai, Z. Zheng and A. Nakayama, "Heat transfer performance analysis on lattice core sandwich panel structures" *Int. J. Heat Mass Transf.*, Vol. 143, No. 118525, pp. 1-12, (2019).
[11] S. Li, Z. Wang and C. Zhou, "Forced convection heat transfer in V-pattern folded core sandwich structures" *Int. J. Aerosp. Eng.*, Vol. 2022, pp. 1–9, (2022).
[12] R. F. Faidallah, M. M. Hanon, Z. Szakál and I. Oldal, "Study of the mechanical characteristics of sandwich structures FDM 3D-printed" *Acta Polytech. Hungarica*, Vol. 20, No. 6, pp. 7–26, (2023).
[13] B. Anwajler, S. Zielińska and A. Witek-Krowiak, "Innovative cellular insulation barrier on the basis of voronoi tessellation—Influence of internal structure optimization on thermal performance" *Materials (Basel).*, Vol. 17, No. 7, pp. 1–19, (2024).
[14] A. A. Nordin, S. N. M. Sofian, S. I. S. Shaharuddin, N. Shaffiar, A. M. A. Hamid and N. A. Sukindar, "A comparison of the thermal conductivity of 3D printed ABS and ABS/Graphite at various infill patterns and densities" M. A. Maleque, A. Z. Ahmad Azhar, N. Sarifuddin, S. I. Syed Shaharuddin, A. Mohd Ali and N. F. H. Abdul Halim, Eds., Singapore: Springer Nature Singapore, pp. 429–435, (2023).
[15] R. Singh, G. S. Sandhu, R. Penna and I. Farina, "Investigations for thermal and electrical conductivity of ABS-Graphene blended prototypes" *Materials (Basel).*, Vol. 10, No. 8, p. 881, (2017).
[16] T. Sonsalla, A. L. Moore, W. J. Meng, A. D. Radadia and L. Weiss, "3-D printer settings effects on the thermal conductivity of acrylonitrile butadiene styrene (ABS)" *Polym. Test.*, Vol. 70, pp. 389–395, (2018).
[17] T. J. Suteja and A. Soesanti, "Mechanical properties of 3D printed Polylactic Acid product for various infill design parameters: A review" *J. Phys. Conf. Ser.*, Vol. 1569, No. 4, pp. 1–6, (2020).
[18] S. A. Khan *et al.*, "Design of a new optimized U-shaped lightweight liquid-cooled battery thermal management system for electric vehicles: A machine learning approach" *Int. Commun. Heat Mass Transf.*, Vol. 136, No. June, p. 106209, (2022).
[19] S. E. Y. Wijayanto, R. Handoko, J. C. Noel, T. W. Anggawirawan and T. J. Suteja, "Identifikasi jenis infill pattern pada proses 3D printing yang menghasilkan hasil cetak dengan kekuatan tekan dan panjang filamen yang optimal" *J. Rekayasa Mesin*, Vol. 13, No. 2, pp. 531–539, (2022).
[20] J. Dobos, M. M. Hanon and I. Oldal, "Effect of infill density and pattern on the specific load capacity of FDM 3D-printed PLA multi-layer sandwich" *J. Polym. Eng.*, Vol. 42, No. 2, pp. 118–128, (2022).
[21] B. Arifvianto, B. E. Satiti, U. A. Salim, A. Nuryanti and M. Mahardika, "Mechanical properties of the FFF sandwich-structured parts made of PLA/TPU multi-material" *Prog. Addit. Manuf.*, Vol. 7, pp. 1213–1223, (2022).
[22] A. Yousefi Kanani and A. Kennedy, "Experimental and numerical analysis of additively manufactured foamed sandwich beams" *Compos. Struct.*, Vol. 312, No. June 2022, p. 116866, (2023).
[23] P. Jongpradist, N. Saingam and P. Tangthamsathit, "Crashworthiness analysis and design of a sandwich composite electric bus structure under full frontal impact" *Heliyon*, Vol. 8, No. 12, p. e11999, (2022).

[24] J. Izdebska-Podsiadły, *Polymers for 3D Printing: Methods, Properties, and Characteristics*. Elsevier, (2022).

[25] J. C. de Camargo, A. J. da Silva Neto, D. C. Knupp, L. A. da Silva Abreu and G. M. de Andrade, "Theoretical and experimental approach with inverse problems for the thermal characterization of parts printed by FDM" *Int. J. Adv. Manuf. Technol.*, Vol. 136, No. 3, pp. 1741–1755, (2025).

[26] S. M. Deivasikamani, K. Mathiyazhagan, G. Mugeshkannan, D. Sridhar and M. Pranesh, "Enhancing Mechanical Characteristics of PETG Carbon Fiber Composite through Various Shell Thickness in FDM Processing" *Int. Res. J. Adv. Eng. Hub*, Vol. 02, No. April, pp. 706–714, (2024).

[27] C. Tosto *et al.*, "Additive Manufacturing of Carbon Fiber Cores for Sandwich Structures: Optimization of Infill Patterns and Fiber Orientation for Improved Impact Resistance" *J. Manuf. Mater. Process.*, Vol. 9, No. 9, pp. 1–24, (2025).

[28] D. Banić, K. Itrić Ivanda, M. Vukoje and T. Cigula, "Impact fracture resistance of Fused Deposition Models from Polylactic Acid with respect to infill density and sample thickness" *Appl. Sci.*, Vol. 14, No. 5, pp. 1–12, (2024).

[29] A. H. Hamzah, L. H. Paijan, M. H. A. Bakar, M. F. Mamat, N. A. Maidin and S. I. Musa, "Effect of wall line count on the mechanical properties of FDM 3D-printed PLA parts" *Malaysian J. Microsc.*, Vol. 20, No. 2, pp. 34–44, (2024).

[30] M. A. Mazlan, M. A. Anas, N. A. Nor Izmin and A. H. Abdullah, "Effects of infill density, wall perimeter and layer height in fabricating 3D printing products" *Materials (Basel).*, Vol. 16, No. 2, pp. 1–11, (2023).

[31] A. S. Bedan, T. F. Abbas and E. A. Hussein, "Prediction and Investigation of the Interactive Impact of Shell Thickness and Infill Density on the Mechanical Properties, and the Mass of ABS Prints" *J. Hunan Univ. Nat. Sci.*, Vol. 50, No. 1, pp. 198–207, (2023).

[32] M. Tychanicz-Kwiecień, S. Grosicki and M. Markowicz, "Experimental Investigation of Thermal Conductivity of Selected 3D-Printed Materials" *Materials (Basel).*, Vol. 18, No. 17, pp. 1–20, (2025).

[33] L. Lopes, D. Reis, A. Paula Junior and M. Almeida, "Influence of 3D microstructure pattern and infill density on the mechanical and thermal properties of PET-G filaments" *Polymers (Basel).*, Vol. 15, No. 10, pp. 1–17, (2023).

[34] K. Khanafer, A. Abbasspour and Y. Aboelkassem, "Thermal conducticity of 3D-printed metal using extrusion-based metal additive manufacturing process" *J. Eng. Mater. Technol.*, Vol. 147, No. 2, pp. 1–23, (2025).

[35] A. Ahmad, A. Abbas, G. Hussain, O. Al-Abbasi, M. Alkahtani and K. Altaf, "Performance evaluation of 3D printed polymer heat exchangers: influence of printing temperature, printing speed and wall thickness with consideration of surface roughness" *Int. J. Adv. Manuf. Technol.*, Vol. 128, No. 7, pp. 3627–3647, (2023).

[36] G. Zorzetto Bittencourt, V. Piccioni, C. Waibel and A. Schlueter, "Surrogate modeling of heat transfer in 3D-printed facades with active learning" *Proc. Build. Simul. 2025 19th Conf. IBPSA*, Vol. 19, (2025).

[37] A. H. Awad, R. Alaa Eldin Sayed and M. Atef, "Enhancing mechanical properties of PETG by optimization of process parameters using the Taguchi method" *J. Phys. Conf. Ser.*, Vol. 3058, No. 1, pp. 1–11, (2025).

[38] B. Beylergil, A. Al-Nadhari and M. Yildiz, "Optimization of Charpy-impact strength of 3D-printed carbon fiber/polyamide composites by Taguchi method" *Polym. Compos.*, Vol. 44, No. 5, pp. 2846–2859, (2023).

[39] M. Z. Baltić *et al.*, "PETG as an alternative material for the production of drone spare parts" *Polymers (Basel).*, Vol. 16, No. 21, pp. 1–20, (2024).

[40] M. Garwacki, I. Cudnik, D. Dziadowiec, P. Szymczak and J. Andrzejewski, "The development of sustainable Polyethylene Terephthalate Glycol-Based (PETG) blends for additive manufacturing processing—The use of multilayered foil waste as the blend component" *Materials (Basel).*, Vol. 17, No. 5, pp. 1–24, (2024).

[41] K. Winters and E. I. L. Jull, "The role of FFF process parameters on impact strength: a review" *Int. J. Adv. Manuf. Technol.*, pp. 3515–3530, (2026).

Copyrights ©2026 The author(s). This is an open access article distributed under the terms of the Creative Commons Attribution (CC BY 4.0), which permits unrestricted use, distribution, and reproduction in any medium, as long as the original authors and source are cited. No permission is required from the authors or the publishers.

**How to cite this paper:**

T. J. Suteja, M. A. Hadiyat and Y. B. Pratiknyo, " Experimental investigation and multi-response optimization of FFF-printed PETG sandwich structure properties for battery casings", *J. Comput. Appl. Res. Mech. Eng.*, Vol. 15, No. 2, pp. 181-198, (2026).

**DOI:** 10.22061/jcarme.2026.113094.2832

**URL:** https://jcarme.sru.ac.ir/?_action=showPDF&article=12634